Pattern Recognition of Barely Visible Impact Damage in Carbon Composites Using Pulsed Thermography

Jia Zhou, Weixiang Du, Lichao Yang, Kailun Deng, Sri Addepalli, and Yifan Zhao, *Senior Member, IEEE*

***Abstract*—This article proposes a novel framework to characterize the morphological pattern of barely visible impact damage using machine learning. Initially, a sequence of image processing methods is introduced to extract the damage contour, which is then described by a Fourier descriptor-based filter. The uncertainty associated with the damage contour under the same impact energy level is then investigated. A variety of geometric features of the contour are extracted to develop an artificial intelligence model, which effectively groups the tested 100 samples impacted by 5 different impact energy levels with an accuracy of 96%. Predictive polynomial models are finally established to link the impact energy to the three selected features. It is found that the major axis length of the damage has the best prediction performance, with an R^2 value up to 0.97. Additionally, impact damage caused by low energy exhibits higher uncertainty than that of high energy, indicating lower predictability.**

***Index Terms*—Artificial intelligence (AI), CFRP, feature extraction, image processing, nondestructive testing (NDT).**

Manuscript received September 18, 2021; revised October 25, 2021; accepted December 4, 2021. Date of publication December 13, 2021; date of current version July 11, 2022. This work was supported in part by the Lloyd's Register Foundation under Grant GA\100113 and in part by the U.K. EPSRC Platform Grant: Through-life performance: From Science to Instrumentation under Grant EP/P027121/1. Paper no. TII-21-4041. *(Jia Zhou and Weixiang Du are co-first authors.) (Corresponding author: Yifan Zhao.)*

Jia Zhou is with the Chengdu Aircraft Industrial (Group) Company, Ltd., AVIC, Chengdu, Sichuan, 610091, China, and also with the School of Aerospace, Transport and Manufacturing, Cranfield University, MK43 0AL Bedfordshire, U.K. (e-mail: jia.zhou@cranfield.ac.uk).

Weixiang Du is with the Gansu Province Special Equipment Inspection and Testing Institute, Lanzhou 730050, China, and also with the School of Aerospace, Transport and Manufacturing, Cranfield University, MK43 0AL Cranfield, U.K. (e-mail: w.du@cranfield.ac.uk).

Lichao Yang, Kailun Deng, Sri Addepalli, and Yifan Zhao are with the School of Aerospace, Transport, and Manufacturing, Cranfield University, MK43 0AL Cranfield, U.K. (e-mail: lichao.yang@cranfield.ac.uk; k.deng@cranfield.ac.uk; p.n.addepalli@cranfield.ac.uk; yifan.zhao@cranfield.ac.uk).

Data is available online at https://doi.org/10.17862/cranfield.rd.17135021

This article has supplementary material provided by the authors and color versions of one or more figures available at https://doi.org/10.1109/TII.2021.3134184.

Digital Object Identifier 10.1109/TII.2021.3134184

I. Introduction

DUE to its excellent material properties such as low density, high strength, corrosion resistance, and high-freedom design characteristics, composite materials play an increasingly essential role in the field of automotive [1] and aviation industries [2]. There is strong evidence that the usage of lighter composites (almost 40% weight reduction [3]) leads to an increase in the fuel efficiency of an aircraft when used in combination with other materials [4]. When the composite material structure receives external impact force such as bird strikes during operation, tool drop during maintenance, or collision during transportation, etc., the composite structure is exposed to a series of stress waves that penetrate the material causing structural damage to the part. Typical damage includes fiber breakage, delamination, matrix cracking, and fiber pull-out. For instance, delamination could be fatal especially when subjected to operational stresses, thus seriously affecting their mechanical performance. Besides, the back-face splitting can reduce the residual strength by as much as 60% [5]. One of the critical delamination type damage is the barely visible impact damage (BVID) [6]. These BVIDs are not easily detectable and cannot be fully characterized visually, thus posing a huge impact on the part's structural integrity leading to catastrophic failure in-service.

As one of the widely used nondestructive testing (NDT) techniques, thermography is rapidly developing as a promising detection technology for composite products during the operation and service phase of the long-life asset [7]. It can detect various defects such as delamination, fiber pull-out, microcracks, crush, and debonding that could be caused by impact damage. Using thermography to detect and analyze BVID has attracted a significant number of studies. A thermographic evaluation procedure was developed for the characterization of impact damage during and after the impact load by determining the size of the heated area [8]. Derusova *et al.* [9] comparatively used active infrared thermography and laser vibrometry to evaluate BVID in Kevlar/carbon composites. A carbon fibre reinforced polymer (CFRP) impact damage inspection method was proposed by Zhang *et al.* [10] based on manifold learning using ultrasonic induced thermography for BVID detection. In these studies, the geometry and the size of damaged areas are usually used to characterize and identify the degree of impact damage in CFRP [11]. It also should be noted that this detection method is still a relatively cumbersome and time-consuming

This work is licensed under a Creative Commons Attribution 4.0 License. For more information, see http://creativecommons.org/licenses/by/4.0/

manual process, which is greatly affected by factors such as the relatively low signal-to-noise ratio and the experience of the inspectors. Besides, composite materials often exhibit anisotropic and nonuniform characteristics, especially when applied to complex geometric structures of aircraft, which leads to a higher uncertainty of damage patterns. This further limits the rapid and robust application of this inspection on composites.

A few studies have been reported in artificial intelligence (AI) based damage detection and characterization of composites using active thermography. Duan *et al.* [12] used the neural network (NN) to analyze infrared images and sort defects including oil, air, and water. In this article, raw data and thermographic signal reconstruction (TSR) coefficients were applied to train and test the two multilayer feedforward NNs. Besides, this article verified the applicability of the NN model to actual experimental data. An intelligent postprocessor was developed by Saeed *et al.* [13] by using a convolutional NN encoding to automatically detect surface defects artificially generated in CFRP samples from a given heat map. A deep feedforward NN algorithm was then used to estimate the depth of the defect of CFRP samples with flat-bottom holes. Iskandarani *et al.* [14] used the energy flow analysis method in MATLAB environment to propose an intelligent prediction method for the damage level of composite materials, which has been proved to be effective. Artificial NNs were used by Benitez *et al.* [15] to reduce the effects of uneven heating and flatness on inspection. They use the thermal contrast curve to detect and evaluate the depth of defects. Dudzik [16] proposed a NN algorithm using active thermal imaging to estimate the depth of defects, where the influence of the emissivity of the sample surface on the estimation accuracy of the defect depth was also explored. Usamentiaga *et al.* [17] introduced a method for automatically detecting the effects of active thermal imaging on CFRP damage. Without manual intervention, defects caused by impact damage can be detected in the infrared image. Iskandarani [18] proposed a method for characterizing and predicting the impact damage of edge structures. However, the literature review suggests that most of the existing AI-based methods in this area are for depth estimation [19] of flat-bottom hole samples or defects classification of artificial defects. Others aimed at developing methods to enhance the captured thermal images [10]. Very limited researches focus on characterizing BVID, particularly on the relationship between the level of impact and the damage contour produced, which is necessary to understand the behavior of the laminate thus providing an estimation of the remaining useful life of the composite part/structure.

This article reports a novel data analysis framework to understand BVID in CFRP caused by various impact energy levels associated with its uncertainty on the impact event itself. A total of 100 samples were produced based on 5 impact energy levels (4, 6, 8, 10, and 12 J) and inspected using pulsed thermography. A pattern recognition method is proposed to understand the uncertainty of the damage contours which are then represented by multiple morphological and moment features. A machine learning-based classifier is then employed to evaluate the classification performance of the energy level based on the extracted features. Predictive models are finally established based on the three selected features from the classification results. Such a model potentially can be used to estimate the impact energy level with the given damage profile or predict the damage profile with the given impact energy level. This article heavily contributes to the research community in the area of AI-enhanced reliability assessment of composites.



Fig. 1. Proposed methodology of this article.

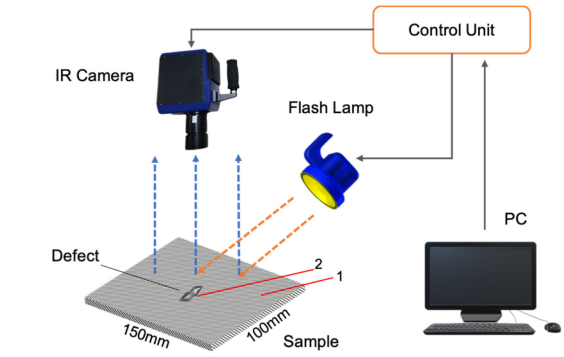
II. Methods

The proposed and implemented methodology of this study is illustrated in Fig. 1. It starts from data collection which contains the preparation of samples and the pulsed thermography inspection. Then, a set of data and image analysis algorithms are applied to characterize the boundary of the impact damage. A variety of features of the damage boundary are then extracted to quantitatively investigate their relationship with the impact energy level. The performance of these features for damage classification is evaluated using a machine learning-based classifier, K-nearest neighbors (KNN). In the last step, polynomial predictive models are used to establish the relationship between the selected features and the impact energy, which could be used for the prediction of geometric features produced by the untrained impact energy. Each step is introduced in the following sections in more detail.

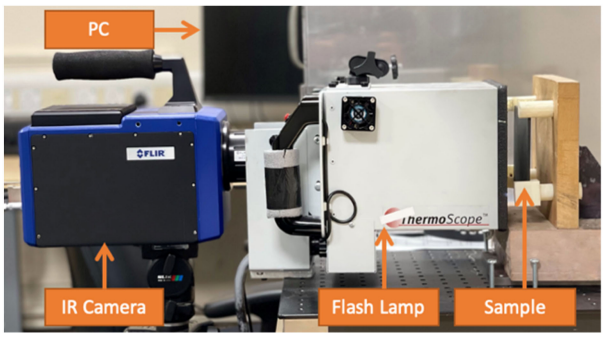
A. Samples and Data Collection

The material specifications of the samples before the impact experiments are as shown in Table I in Supplementary. After being hand-laid and cured, four 750 × 750 × 3 mm plates were manufactured, marked as P1, P2, P3, and P4, respectively. Then they were cut into multiple samples with a size of 150 × 100 × 3 mm. The impact experiments with predetermined energy levels were performed on each sample. The impact energy is generated by a hemispherical indenter weighing 2.281 kg, which performs free drop under acceleration of gravity. By accurately setting the drop height of the weight, the impact energy of 4, 6, 8, 10, and 12 J was obtained, respectively. Each plate contributed five specimens for each impact energy level.

As illustrated in Fig. 2, during the pulsed thermographic inspection working under the reflection mode, a short- and high-energy light pulse from a flash lamp is projected onto the sample surface. Heat conduction then takes place from the heated surface to the interior of the sample, leading to a continuous decay in the surface temperature. An infrared (IR) radiometer controlled by a computer captures the time-dependent response of the sample surface temperature (decay profile). In areas of the sample surface above a defect [see point 2 in Fig. 2(a)] the transient flow of heat from the surface into the sample bulk is wholly or partially separated, thus causing a temperature deviation from the sound areas, where the sample continues to cool until it reaches the sample back wall [see point 1 in Fig. 2]. Most of the defect detection methods are based on the analysis of these temperature decay curves.



(a)



(b)

Fig. 2. (a) Experimental configuration of the pulsed thermographic inspection under the reflection mode, where point 1 denotes a sound area on the sample surface and point 2 denotes a position with defects underneath. (b) Photo of the experimental setup.

In this article, the Thermoscope II pulsed-active thermography system is used. It comprises two capacitor banks powered Xenon flash lamps mounted in an internally reflective hood and a desktop PC to capture and store data. A FLIR SC7000 series IR radiometer operating under 3–5.1 μm and a spatial resolution of 640 $\times$ 512 pixels was used to perform the inspection. The samples were placed with their surface perpendicular to the IR camera's line of sight at 250 mm from the lens. The applied energy was approximately 2 kJ over an inspection area of 250 $\times$ 200 mm. The pixel pitch is 0.32 mm. Considering the thickness of the samples and the low thermal diffusivity of CFRP, a sampling rate of 50 Hz was used, and a total of 1000 frames, equivalent to a 20 s data length, were captured.

B. Damage Characterization

The proposed process to characterize the impact damage of composites can be divided into two parts: damage contour extraction and uncertainty characterization. Focusing on an individual sample, the first part extracts the contour of impact damage. The second part aims to investigate the contour variation of different samples under the same impact energy and same plate, contour comparison of the samples under different impact energies and same plate, and the contour variation of samples coming from multiple plates manufactured using the same process under the same impact energy.

1) Damage Contour Extraction: The whole process of damage contour extraction can be illustrated in Fig. 3. This article proposes to use the adaptive peak temperature contrast (APTC) method to detect defects [20]. For each pixel on the image plane, the peak of temperature contrast by time is computed and a map of these peak values is constructed to represent the detected damage. Thus, damage with different sizes or depths can be visualized achieving maximal contrast in a single image. To reduce the noise, the TSR algorithm [21] is employed to fit the raw data using a sixth-order polynomial before the application of APTC. An example outcome of TSR is shown in Fig. 3(a). The estimation of APTC can be written as follows:

$$APTC\left(x,y\right)=\max_{t}\left(\tilde{T}\left(x,y,t\right)-\tilde{T}_{A_s}\left(t\right)\right) \tag{1}$$

where $\tilde{T}$ denotes the TSR fitting of the raw temperature, which can be expressed as follows:

$$\tilde{T}\left(x,y,t\right)=\exp\left(\sum_{i=0}^{n}a_i(\ln\left(t\right))^i\right) \tag{2}$$

where n is the model order, t is the time, and a_i the fitted coefficient of the data collected from the position (x,y). $\tilde{T}_{A_s}(t)$ denotes the averaged TSR fitting for the sound area. The selection of the model order is discussed by Zhao *et al.* [22]. In all examples of this article, the model order was chosen as 7 as it achieved the highest contrast. The first derivative of APTC ($APTC1D$) is then calculated and used to further enhance damage and is written as follows:

$$APTC1D\left(x,y\right)=\max_{t}\left(\frac{d\left(\tilde{T}\left(x,y,t\right)\right)}{dt}-\frac{d\left(\tilde{T}_{A_s}\left(t\right)\right)}{dt}\right). \tag{3}$$

It should be noted that the first derivative is computed using the fitted coefficients a_i to achieve better time resolution than using the raw data. An example outcome of APTC is shown in Fig. 3(b).

After the damage enhancement, a confidence map approach [20] is employed to transfer the intensity of damage images into the confidence level of inspection to better represent damage. This process allows improved visualization of complex damage with different depths in a single image even when $APTC1D$ is significantly different. The mean and standard deviation of $APTC1D$, denoted by $\overline{\mu_p}(i)$ and $\overline{\sigma_p}(i)$, respectively, are estimated by randomly sampling the pixels from the defined sound areas with the number of sampled pixels (N). For each considered pixel of each trial, the z^* value can be estimated by

$$z^*\left(x,y,i\right)=\frac{\left|APTC1D\left(x,y,i\right)-\overline{\mu_p}\left(i\right)\right|}{\overline{\sigma_p}\left(i\right)}. \tag{4}$$

To reduce the uncertainty caused by random sampling, the process of sampling and calculation of z^* is repeated for Q times and the z^* values for each trial are fused using the "OR" operator, written as follows:

$$z^*\left(x,y,i\right)=\bigcup_{j=1}^{Q}\frac{\left|APTC1D\left(x,y,i,j\right)-\overline{\mu_p}\left(i,j\right)\right|}{\overline{\sigma_p}\left(i,j\right)}. \tag{5}$$

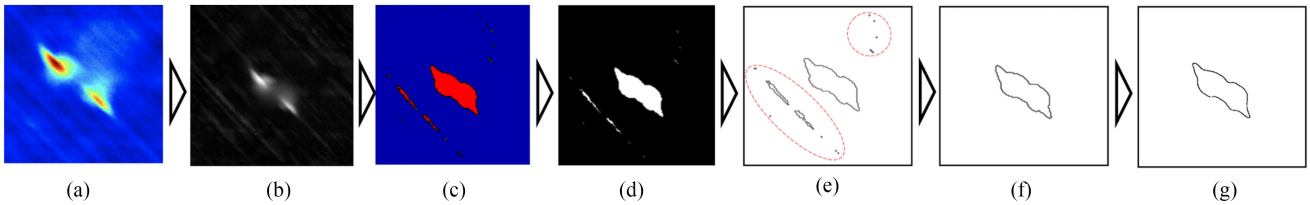


Fig. 3. Proposed process to extract impact damage contour. (a) TSR. (b) APTC. (c) Confidence map. (d) Binarization. (e) Contour extraction. (f) Connected components analysis. (g) Fourier descriptor.

The confidence map is then produced by mapping the z^* value into a confidence level, shown in Table II in Supplementary. An example of a confidence map is shown in Fig. 3(c). A threshold of 95% confidence level is then used to convert the damage into a binary form [see Fig. 3(d)]. The contour can be easily extracted based on this binary image [see Fig. 3(e)]. However, it can be observed that noise can appear around the true damage due to interference from surface damage or an inappropriate threshold. To remove the spatial noise, an image segmentation method, called the connected component analysis, is utilized to select the damage contour with the largest area, the result of which is demonstrated in Fig. 3(f).

Furthermore, sharp corners can be observed in the extracted contour, as shown in Fig. 3(f). It is proven in the later steps that such noise will significantly affect the accuracy of the AI classification. In this article, we propose to use Fourier descriptors-based filter [23] to smooth the boundary. The contour boundary can be represented by a coordinate sequence with K elements. Each coordinate pair (x and y) can be treated as a complex number, shown as follows:

$$s(k) = x(k) + jy(k) \tag{6}$$

where the x-axis is treated as the real component and the y-axis as the imaginary component and $k = 12, \ldots, K$. Then, fast Fourier transform (FFT) is performed on $s(k)$ so that the Fourier descriptors of the contour, called $a(u)$, can be represented as follows:

$$a(u) = \sum_{k=1}^{K} s(k)\, e^{-j2\pi uk/K}. \tag{7}$$

The first $P(P < K)$ Fourier descriptors, representing the low-frequency component or smooth boundary, are then preserved and the remaining $K - P$ descriptors are neglected. The inverse FFT is then performed to reconstruct the contour, written as follows:

$$\hat{s}(k) = \frac{1}{K} \sum_{u=1}^{P} a(u)\, e^{j2\pi uk/K}. \tag{8}$$

We use the ratio of K and P to control the smoothness, written as follows:

$$r = K/P. \tag{9}$$

Different values of r have been tested in this study and it has been found that the highest classification accuracy is achieved when r is chosen as 30. An example outcome of FFT filtering is shown in Fig. 3(g).

2) Contour Uncertainty Characterization: After obtaining the contour for a single sample, the contours of all samples of the same energy level in the same plate are superimposed, using the centroid of each contour as a reference. It should be noted that different plates may have slight structural differences due to the variation associated with the manufacturing processing itself. Different orientations of damage patterns have been observed for different plates. An example output of this step can be found in Fig. 4(a). Then, the outermost boundary of the contour overlay, and the innermost boundary are extracted and the gap between is filled by assigning values to pixels of 0. Such a band, as shown in Fig. 4(b), illustrates the potential damage boundary for a certain impact energy level. To calculate the average contour for a specific impact energy level, the skeleton of the band is extracted using the function *bwmorph* in MATLAB. An example output of this step can be found in Fig. 4(c), where some branches can be observed. To remove those branches, the closed operation is implemented. Then, the filter using Fourier descriptors, described in the earlier section, is applied here again to smooth the boundary, the result of which is demonstrated in Fig. 4(d). The mean curve of each impact energy level can then be overlayed to reveal how the impact energy leads to different damage profiles, as shown in Fig. 4(e). The contour band, shown in Fig. 4(b), can also be overlayed to evaluate the uncertainty of damage pattern against different impact energy levels, as shown in Fig. 4(f).

C. Feature Extraction

To apply machine learning classifiers to quantitatively analyze the difference and similarity of impact damage patterns associated with impact energy, this feature extraction step aims to represent the damage patterns using a variety of singular values. This study considers two groups of features including geometric features and cosine similarity.

A total of 6 geometric features, shown in Table III in Supplementary and illustrated in Fig. 5, are produced. *Area*, *Perimeter*, and *Major Axis Length* are the parameters that are used to describe the size of an object. Orientation describes the angle between the *Major Axis Length* and the x-axis in the image plane. Eccentricity and circularity describe the shape of the objects. In mathematics, the eccentricity of a conic section is a non-negative real number that uniquely characterizes its shape. The eccentricity of a circle is zero, while the eccentricity of an

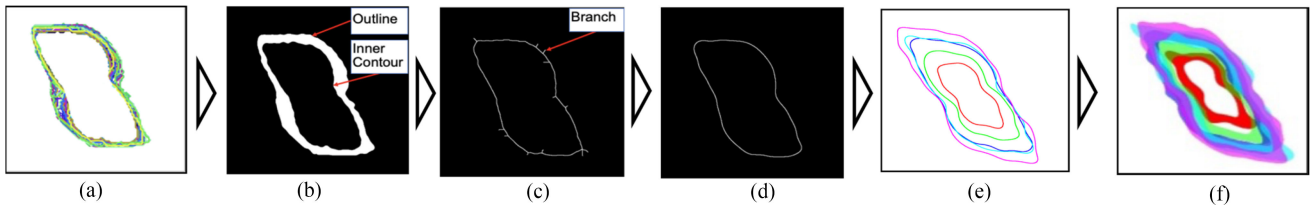


Fig. 4. Proposed process to characterize the contour uncertainty. (a) Multiple contours overlay. (b) Contour extraction and filling. (c) Skeleton extraction. (d) FFT. (e) Mean curves overlay. (f) Confidence Bands overlay.

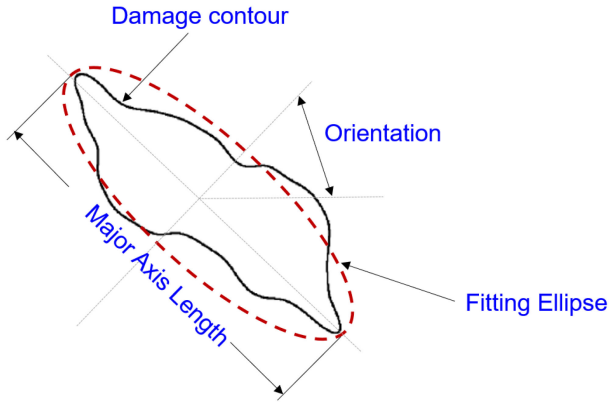


Fig. 5. Illustration of geometric features.

ellipse which is not a circle is greater than zero but less than 1. Circularity, also referred to as roundness, is the measure of how closely the shape of an object approaches that of a mathematically perfect circle.

Cosine similarity is a measure of the similarity between two nonzero vectors of an inner product space. It is a judgment of orientation and not magnitude: two vectors with the same orientation have a cosine similarity of 1, two vectors oriented at 90° relative to each other have a similarity of 0, and two vectors opposed have a similarity of −1, independent of their magnitude. Given two vectors of attributes (contour for this study), A and B, the cosine similarity is calculated by

$$\cos(\theta) = \frac{\sum_{i=1}^{n} A_i B_i}{\sqrt{\sum_{i=1}^{n} {A_i}^2}\sqrt{\sum_{i=1}^{n} {B_i}^2}} \tag{10}$$

where A_i and B_i are components of vectors A and B, respectively. Initially, the image is divided into eight by eight blocks. The averaged grey value of each block is calculated and used to construct the 1-D vectors A or B by connecting all 64 (n) values.

Some other geometric features, such as centroid and Euler number, and scale invariants, such as Hu Moments, have been extracted and analyzed in this article (shown in Supplementary), there is no significant findings consider that the introduced six features have the right balance to evaluate the damage shape similarity among different groups and the trend of dimension change following the increase of impact energy level.

D. AI Training and Model Validation

The KNN algorithm was applied to perform the classification of the selected features. During the initial development of classification solutions, different machine learning algorithms were analyzed, such as support vector machine, decision tree, and KNN. KNN tended to present performance superiority in this study when compared with other methods and was selected as the main classifier in this article. The function "Fine KNN" in MATLAB, where K is set to 1, was used as it showed the best classification accuracy. As the most popular way to measure the distance in KNN, Euclidean distance was applied because of its superior interpretability and performance. A large K value can reduce the impact of noise on classification based on KNN, making the boundaries between classes less obvious. In this experiment, we observed that the Euclidean distance among these groups is relatively small; therefore, a large K value cannot distinguish them well and $K = 1$ is chosen.

The dataset was divided into ten subsets and then cross-validation was undertaken. For each iteration of the 10-fold cross-validation, different subsets are used for training and testing. In the first iteration, the first subset is used for testing and the remaining subsets are used for training. The second iteration uses the second subset for testing and so on. To obtain the final result, an average of ten classification accuracies are computed. Each accuracy comes from a single iteration of k-fold cross-validation. The 10-fold cross-validation is performed five times by reshuffling data to gather five results statistically for each classification task. To further evaluate the machine learning performance, this article uses accuracy (Accu), defined as follows:

$$Accu = \frac{TP + TN}{TP + TN + FP + FN} \times 100\% \tag{11}$$

where TP = true positive, FN = false negative, TN = true negative, and FP = false positive.

III. Results

A. Impact Damage Contour

Fig. S1 in supplementary shows the contour overlay of the samples impacted by the five energy levels within the same plate. The impact damage exhibits a butterfly shape around the dent. The size of damage increases following the increment of energy level, which is consistent for all the plates. Overall, the damage pattern is consistent in terms of shape and orientation for the

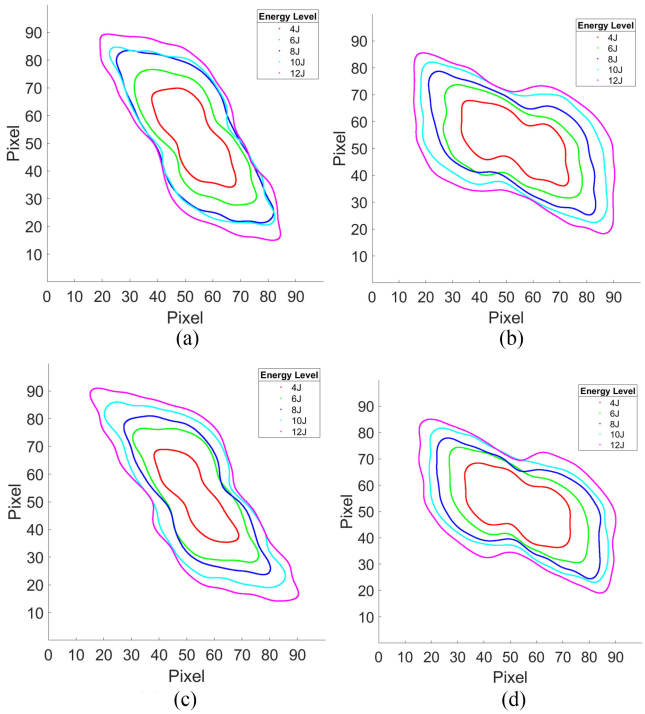


Fig. 6. Mean contour overlay. (a) Plate 1. (b) Plate 2. (c) Plate 3. (d) Plate 4.

samples with the same energy level and plate, although small variation can be observed, particularly the area around the dent for low energy levels (e.g., 4 J impact samples). The length from the west–north tip to the east-south tip is quite consistent for the same energy level. For the same energy level, the damage across different plates has different orientations, whereas the orientation for the same plate but with different energy levels is almost the same. This observation suggests a potential variation of the fiber layout of the samples, which affects the growth of delamination. In terms of the percentage of variation, the uncertainty of the damage profile for the low energy level seems to be larger than that of the high impact energy level. In other words, the damage is more predictable for high-impact energy than low-impact energy.

To better illustrate the change of the impact damage caused by different energy levels, Fig. 6 shows the mean contour overlay for the four plates. It can be observed that with the increasing impact energy, the tips at the west-north and east-south directions grow faster than in other directions. Plates 1 and 3 have a similar pattern, whereas Plates 2 and 4 are similar. There is almost no overlap or crossover in the mean contour between different energy levels except 8 and 10 J in Plate 1, which suggests a potential high classification accuracy based on the damage contour. To further investigate the variation of different samples and different energy levels, Fig. 7 illustrates the contour bands, where different colors indicate different energy levels. Overall, the patterns of the five energy levels are distinguishable, although there is some overlapping between adjacent energy levels, particularly for 10 and 12 J.

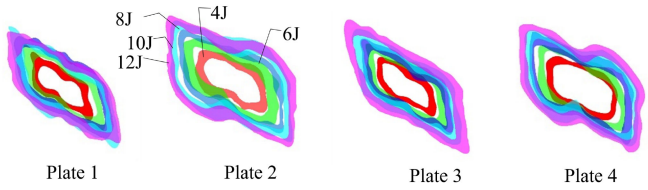


Fig. 7. Contour band overlay for different plates.

B. Features

Fig. 8 plots the boxplots for six geometric features against the impact energy level. It is clear that *Area*, *Perimeter*, and *Major Axis Length* increase following the increment of energy level, except 8 and 10 J of Plate 1 which could be due to the close range of the impact event itself combined with the manufacturing process parameter variations coming from the manual lay-up stage. The relationship is almost positive linear for *Area*, which has been reported in previous research [20], [24]. *Perimeter* vs energy and *Major Axis Length* vs energy are with a positive square root relationship. For Plates 2 and 4, the standard variations of *Major Axis Length* are significantly smaller than those of Plates 1 and 3, which suggests a better classification of different energy levels. The standard variations for *Perimeter* and *Area* are relatively larger and consistent across the four plates. For the features of shape including *Circularity* and *Eccentricity*, the values are similar for different energy levels. The values for different plates have no significant difference. This observation suggests that the shape of impact damage is predictable and almost independent of the energy level. For the *Orientation*, the values of Plates 1 and 3 are similar while the values of Plates 2 and 4 are similar. However, there is about a 30° difference between Plates 1 and 2. All these observations are consistent with those from Figs. 6 to 7.

Fig. 9 shows the pairwise cosine similarity of the energy level for all samples. Overall, the values are high and similar, which suggests that there is a high degree of predictability of the damage pattern. For the comparison of the contours from the same energy level, the similarities from the highest to the lowest are 12 J vs 12 J, 10 J vs 10 J, 8 J vs 8 J, 6 J vs 6 J, and 4 J vs 4 J. That is, the higher the energy level, the higher the similarity of the contour formed. It suggests a higher uncertainty of damage pattern caused by the low energy level. In other words, the damage pattern caused by the high-energy level is more predictable. For the comparison of the contours between different energy levels, 4 J vs 6 J, 6 J vs 8 J, and 4 J vs 8 J have the lowest similarity, which again demonstrates the relatively higher uncertainty or lower predictability of damage profile for low impact energy levels. This observation is understandable because the damage profile is influenced by multiple factors, such as energy, experiment uncertainty, and material layout. The weight of each influence factor will change with the increase of the energy level, and the high-level energy may have a greater weight on the damage profile, which leads to a lower uncertainty level.

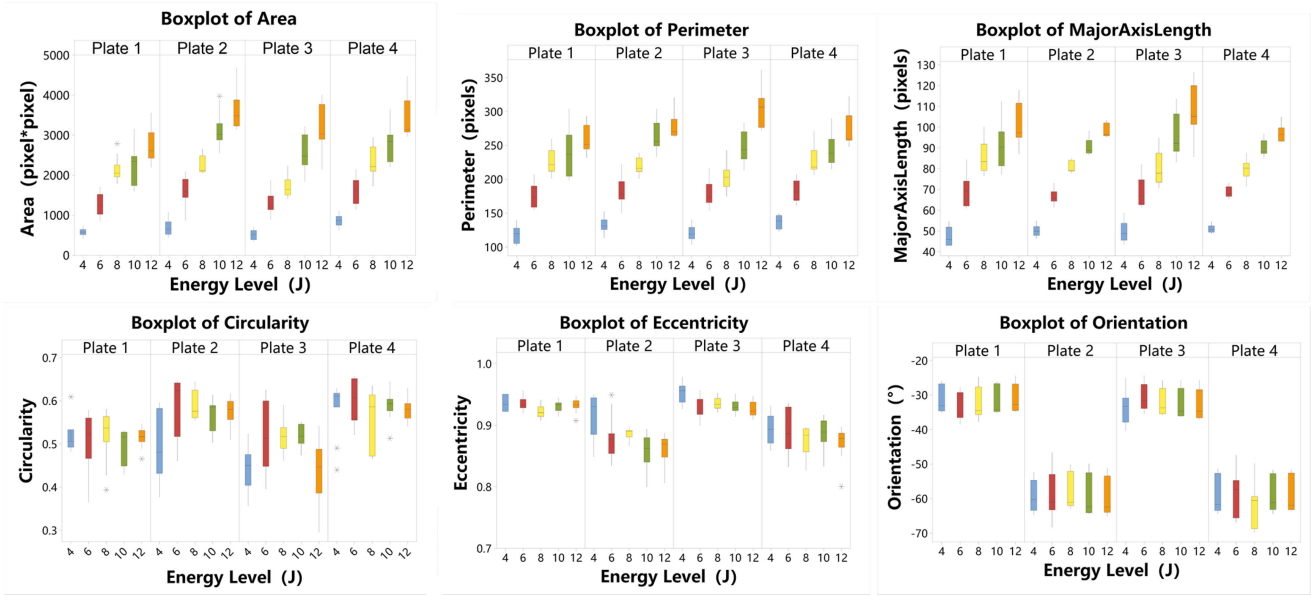


Fig. 8. Boxplots of the extracted geometric features.

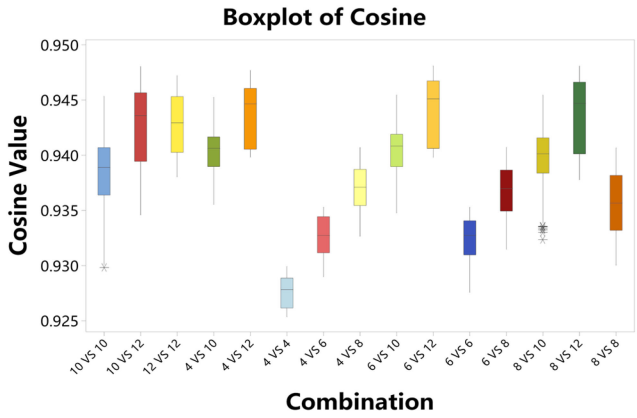


Fig. 9. Boxplots of the extracted cosine similarity for all plates.

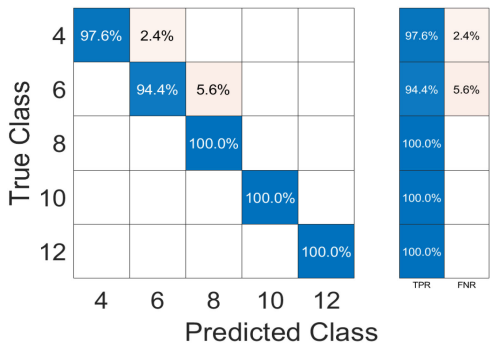


Fig. 10. Confusion matrix using all geometric features.

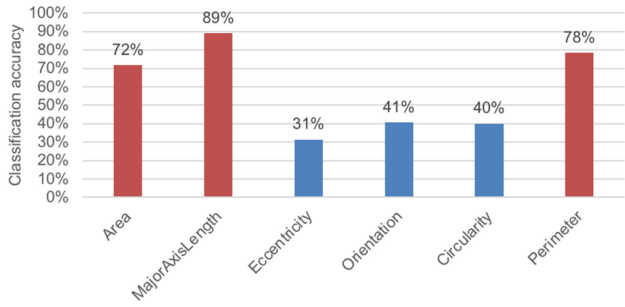


Fig. 11. Classification accuracy using individual geometric feature.

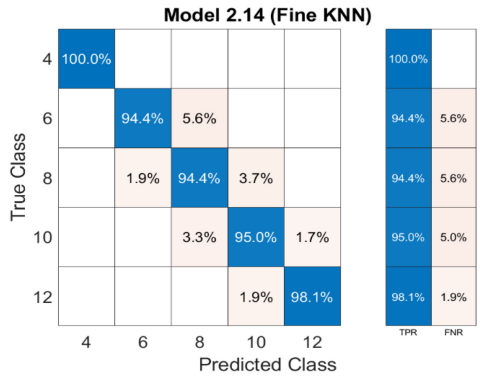


Fig. 12. Confusion matrix using three selected features (*area*, *perimeter*, and *major axis length*).

C. Classification

This section reports the quantitative performance of the classification of the extracted geometric features. Fig. 10 shows the confusion matrix of the cross-validation using all geometric features. A value higher than 94% accuracy is achieved for all the five energy levels with 8, 10, and 12 J showing a 100% accuracy, thus confirming the previous observation that the damage pattern caused by the high-energy levels is more predictable. Additionally, to demonstrate the necessity of the FFT filter to smooth the contour, Fig. S2 in Supplementary shows the confusion matrix without this filter. The classification accuracy for 8 J now drops to

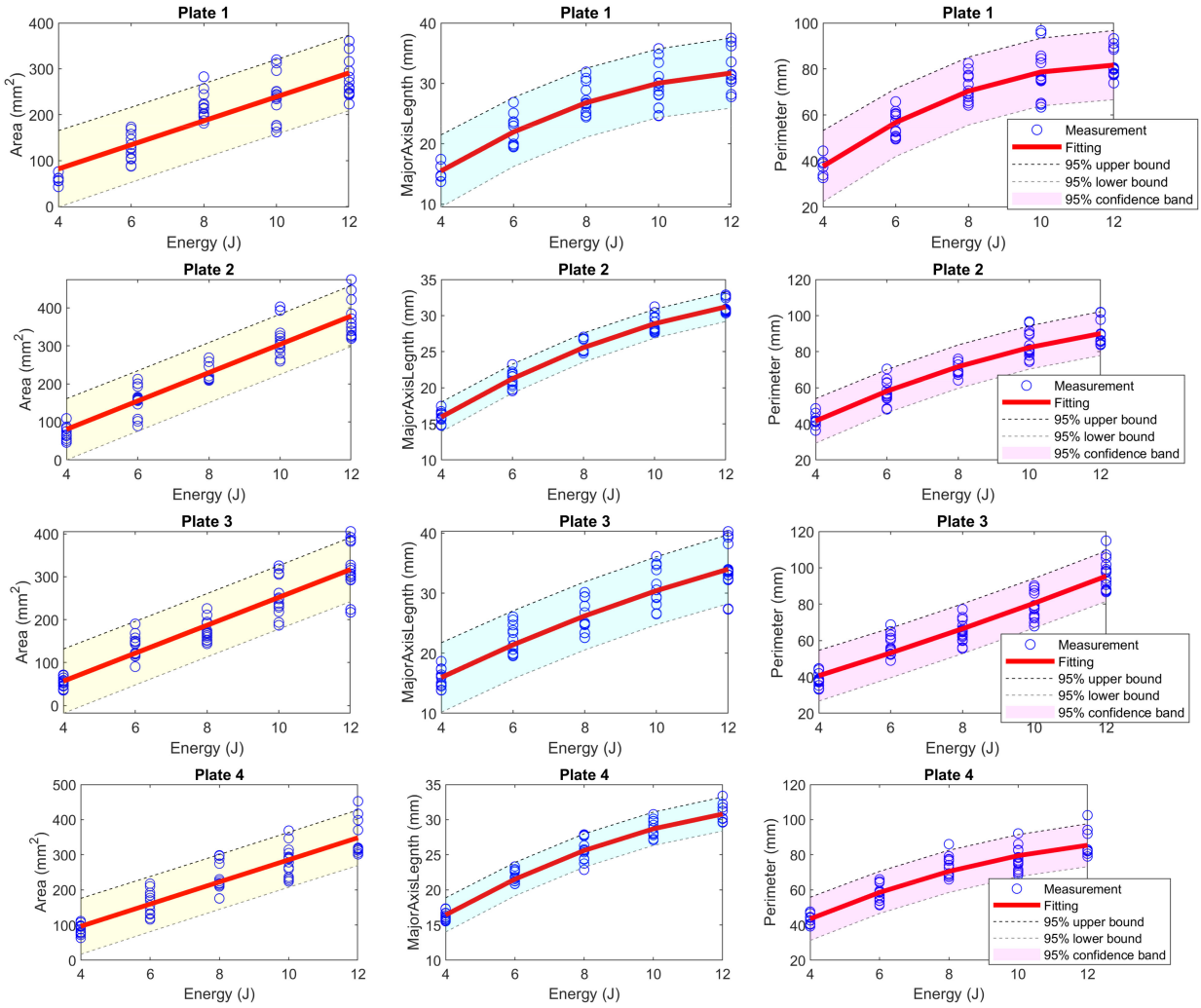


Fig. 13. Predictive modeling for three selected geometric features.

83%. The performance of higher impact energy levels is affected significantly.

Fig. 11 plots the classification performance using an individual feature, where it can be observed that the *Major Axis Length* tops the performance with an accuracy of 89%, followed by the *Perimeter* at 78% and the *Area* at 72%. It is expected that the three shape-related features have a low accuracy level (<41%) because of the similarity of damage patterns for different impact damage levels. Finally, the three features with high accuracy are chosen to produce the final model, the result of which is shown in Fig. 12. The five groups can be distinguished with an average accuracy of 96.36%. It should be noted that the deep learning method has been applied on the labeled contour images for comparison, but its accuracy is significantly lower, which could be caused by the limited sample number.

D. Predictive Modeling

One limitation of the established machine learning model is that it is not predictive because it cannot recognize the damage caused by un-trained energy levels. A linear or nonlinear polynomial model can be used to model the relationship between the energy level and the selected geometric features. The model can be written as follows:

$$F = \sum_{i=0}^{N} p_i E^i \tag{12}$$

where F is the geometric feature, E is the impact energy, and N is the model order. Considering the observation in Fig. 8, N is chosen as 1 for *Area* and 2 for *Perimeter* and *Major Axis Length*. The fitting models for three selected geometric features are shown in Fig. 13 and Table IV in Supplementary. The model performance is evaluated by R2. For all four plates, the model performance based on *Area* shows no significant difference, and the average value of R2 is 0.79. Again, the *Major Axis Length* achieves the highest model prediction accuracy with an R2 value of 0.86. Particularly for Plates 2 and 4, the R2 values are higher than 0.95. The 95% confidence bands of Plates 2 and 4 are narrower than those of Plates 1 and 3. The *Perimeter* achieves an intermediate performance with an R2 value of 0.84. The models

shown in Table IV in Supplementary can be used to estimate the geometric features for untrained impact energy.

E. Discussion

The proposed framework allows us to understand impact damage using feature engineering and shallow machine learning approaches. Compared with existing deep learning-based approaches used in this topic, the proposed method tends to be transparent and aims to reveal which geometric features are dependent or independent on the impact energy level. Such a method allows us to develop a model to predict damage profile caused by an impact energy level that has not been tested. It should be noted that this analytics framework tends to be general for different NDTs. Steps (1) and (2) in Fig. 3 are specific for pulsed thermography and can be replaced by other damage detection methods. Steps (3) to (7) in Figs. 3 and 4 tend to be general for large damage (not appropriate for cracks). They are all image-processing based so it is applicable for data from other NDTs, as long as the data can be visualized as images.

One potential technical limitation is that, in Fig. 3(d), to convert the damage profile into a binary form, a confidence threshold must be chosen manually or automatically. It could be subjective and the variation of this could lead to different damage profiles, particularly for damage areas with a low confidence level. Moreover, how many geometric features should be included to produce the highest classification accuracy or best predictive model still requires further exploration. Some feature reduction methods, such as Principal Component Analysis, could be tested to select the concise features since some information is probably overlapped among the extracted features. Another limitation of this study is that the number of samples and the variation of impact damage could be increased by introducing more impact energy levels, particularly the low energy level, and different impact mechanisms, to push the applicable boundary of the parametric modeling. It could also enable the application of deep learning methods. Further work can also focus on the prediction of impact damage patterns when the energy level is not known previously. In other words, based on the detected damage and the morphological characterization, we could potentially estimate the impact energy, thereby reducing the severity of the damage that is created. We believe this will significantly improve the in-service maintenance of these advanced composites. Additionally, we also aim to investigate the influencing factors on impact damage patterns.

IV. Conclusion

This article reported a novel data analysis framework for investigating composite BVID associated with the impact energy using pulsed thermography. The framework was featured with a new contour extraction and description process, contour uncertainty evaluation, a variety of carefully selected features, and a machine learning-based classifier. The following conclusions were drawn based on the results through testing 100 samples evenly distributed across the five impact energy levels.

1) Very similar geometric patterns of impact damage, in the form of butterfly shape, have been observed for all the samples. They exhibit similar circularity and eccentricity. The area of damage linearly increased following the increase in impact energy level.
2) There was more uncertainty of the damage contour caused by low energy level, particularly on the area around the impact dent, whereas the contour for high-energy level was more predictable. This was due to the fundamental proportionality that a higher impact energy level leads to larger damage.
3) *Major Axis Length* was the best feature to distinguish these five groups of samples with an accuracy of 89%. *Area* and *Perimeter* were the next two good features.
4) The three selected geometric features can effectively classify the impact damage pattern using a machine learning classifier with an overall accuracy $>90\%$.
5) Using a Fourier descriptor-based filter can not only smooth the impact damage contour but also improve the classification accuracy.
6) The orientation of the damage profile was affected by the fiber layout. In other words, the uncertainty of damage pattern was larger for samples even when they come from the same manufacturing process due to the variations coming from the heterogeneity and anisotropy of the material itself.

References

[1] F. Ferreira, I. Pinheiro, S. de Souza, L. Mei, and L. Lona, "Polymer composites reinforced with natural fibers and nanocellulose in the automotive industry: A short review," *J. Composite Sci.*, vol. 3, no. 2, May 2019, Art. no. 51.

[2] G. Kamali, "Advanced composite materials of the future in aerospace engineering," *Int. J. Res. Appl. Sci. Eng. Technol.*, vol. V, no. II, pp. 610–614, Feb. 2017.

[3] J. Zhang, K. Chaisombat, S. He, and C. H. Wang, "Hybrid composite laminates reinforced with glass/carbon woven fabrics for lightweight load bearing structures," *Mater. Des.*, vol. 36, pp. 75–80, Apr. 2012.

[4] B. Alemour, O. Badran, and M. R. Hassan, "A review of using conductive composite materials in solving lightening strike and ice accumulation problems in aviation," *J. Aerosp. Technol. Manage.*, vol. 11, Mar. 2019, Art. no. 1.

[5] T. Mitrevski, I. H. Marshall, and R. Thomson, "The influence of impactor shape on the damage to composite laminates," *Composite Struct.*, vol. 76, no. 1–2, pp. 116–122, Oct. 2006.

[6] M. Saeedifar, M. A. Najafabadi, D. Zarouchas, H. H. Toudeshky, and M. Jalalvand, "Barely visible impact damage assessment in laminated composites using acoustic emission," *Composite Part B Eng.*, vol. 152, pp. 180–192, Nov. 2018.

[7] W. Du, H. Liu, Y. Zhao, A. Sirikham, S. Addepalli, and Y. Zhao, "A miniaturised active thermography system to inspect composite laminates," *IEEE Trans. Ind. Informat.*, vol. 17, no. 5, pp. 3314–3323, May 2020.

[8] C. Maierhofer, R. Krankenhagen, and M. Röllig, "Application of thermographic testing for the characterization of impact damage during and after impact load," *Composite Part B Eng.*, vol. 173, Sep. 2019, Art. no. 106899.

[9] D. A. Derusova, V. P. Vavilov, A. O. Chulkov, B. I. Shagdirov, N. Saeed, and M. Omar, "Evaluating impact damage in Kevlar/carbon composites by using laser vibrometry and active infrared thermography," *Electron. Lett.*, vol. 56, no. 19, pp. 1001–1003, Sep. 2020.

[10] X. Zhang *et al.*, "CFRP impact damage inspection based on manifold learning using ultrasonic induced thermography," *IEEE Trans. Ind. Informat.*, vol. 15, no. 5, pp. 2648–2659, May 2019.

[11] A. Hauffe, F. Hähnel, and K. Wolf, "Comparison of algorithms to quantify the damaged area in CFRP ultrasonic scans," *Composite Struct.*, vol. 235, Mar. 2020, Art. no. 111791.

[12] Y. Duan *et al.*, "Automated defect classification in infrared thermography based on a neural network," *NDT E Int.*, vol. 107, Oct. 2019, Art. no. 102147.

[13] N. Saeed, N. King, Z. Said, and M. A. Omar, "Automatic defects detection in CFRP thermograms, using convolutional neural networks and transfer learning," *Infrared Phys. Technol.*, vol. 102, Nov. 2019, Art. no. 103048.
[14] M. Z. Iskandarani, "A novel approach to analyze impact damage in composite structures using optical flow cross correlation with neural networks (N-OFCC)," in *Proc. Comput. Conf.*, 2017, pp. 615–619.
[15] H. D. Benitez, C. Ibarra-Castanedo, A. Bendada, X. Maldague, H. Loaiza, and E. Caicedo, "Defect quantification with reference-free thermal contrast and artificial neural networks," *Proc. SPIE*, vol. 6541, Apr. 2007, Art. no. 65410V.
[16] S. Dudzik, "Analysis of the accuracy of a neural algorithm for defect depth estimation using PCA processing from active thermography data," *Infrared Phys. Technol.*, vol. 56, pp. 1–7, Jan. 2013.
[17] R. Usamentiaga, P. Venegas, J. Guerediaga, L. Vega, and I. López, "Feature extraction and analysis for automatic characterization of impact damage in carbon fiber composites using active thermography," *NDT E Int.*, vol. 54, pp. 123–132, Mar. 2013.
[18] M. Iskandarani, "Data encoding and reconstruction of thermal imaging maps of impact damaged composite structures using feature space and neural networks," in *Proc. MATEC Web Conf.*, 2019, Art. no. 03008.
[19] Q. Yi, H. Malekmohammadi, G. Y. Tian, S. Laureti, and M. Ricci, "Quantitative evaluation of crack depths on thin aluminum plate using Eddy current pulse-compression thermography," *IEEE Trans. Ind. Informat.*, vol. 16, no. 6, pp. 3963–3973, Jun. 2020.
[20] Y. Zhao, S. Addepalli, A. Sirikham, and R. Roy, "A confidence map based damage assessment approach using pulsed thermographic inspection," *NDT E Int.*, vol. 93, pp. 86–97, Jan. 2018.
[21] S. M. Shepard, "Reconstruction and enhancement of active thermographic image sequences," *Opt. Eng.*, vol. 42, no. 5, May 2003, Art. no. 1337.
[22] Y. Zhao, J. Mehnen, A. Sirikham, and R. Roy, "A novel defect depth measurement method based on nonlinear system identification for pulsed thermographic inspection," *Mech. Syst. Signal Process.*, vol. 85, pp. 382–395, Feb. 2017.
[23] R. C. Gonzalez and R. E. Woods, *Digital Image Processing*. Englewood Cliffs, NJ, USA: Prentice-Hall, 2007.
[24] Y. Zhao, J. Mehnen, W. Xu, M. Alrashed, S. Abineri, and R. Roy, "Degradation assessment of industrial composites using thermography," *Procedia CIRP*, vol. 38, pp. 147–152, 2015.



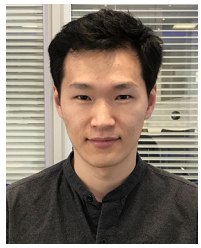
Jia Zhou received the B.S. degree in mechanical design and manufacturing and its automation from Southwest Jiaotong University, Chengdu, China, in 2013, and the M.Sc. degree in manufacturing technology and management from Cranfield University, Cranfield, U.K., in 2020.

He is currently engaged in the research of nondestructive testing technology based on computer vision in the aviation industry.

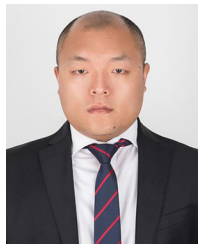


Weixiang Du received the M.Sc. degree in mechanical engineering from the University of Portsmouth, Portsmouth, U.K., in 2014, and the Ph.D. degree in manufacturing from Cranfield University, Cranfield, U.K., in 2021.

He has been an Engineer working with Gansu Special Equipment Inspection and Testing Research Institute for ten years. His current research interests include the areas of NDT methods, especially miniaturized NDT techniques for in-situ inspection.



Lichao Yang was born in Shanxi, China. He received the M.Sc. degree in automotive mechatronics in 2018 from Cranfield University, Cranfield, U.K., where he is currently working toward the Ph.D. degree in driver nondriving activities analysis with the Centre for Life-cycle Engineering and Management.



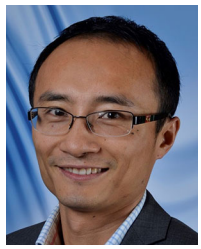
Kailun Deng received the B.Eng. degree in industrial design from the Beijing Institute of Technology, Beijing, China, in 2011, and the M.Sc. degree in engineering and management of manufacturing systems in 2018 from Cranfield University, Cranfield, U.K., where he is currently working toward the Ph.D. degree in manufacturing.

During his studies for master's degree, he focused on manufacturing process optimization and management improvement for manufacturing enterprises. He is currently working with Cranfield University on improving nondestructive Testing (NDT) techniques using the project is to develop an intelligent pulsed thermographic inspection system powered by artificial intelligence (AI) and augmented reality (AR) technologies to improve its detectability and efficiency.



Sri Addepalli received the B.Eng. degree in mechanical engineering from Anna University, Chennai, India, in 2006, and the M.Phil. degree in materials technology from Swansea University, Swansea, U.K., in 2010.

He is currently a Lecturer in Degradation Assessment with Cranfield University, Cranfield, U.K. He is also a CSWIP Certified Level 1 Thermography Inspector and a Full-Time Professional Member of the Institute of Engineering Technology (MIET). His research interests include passive and active thermography and material/component damage characterization with specific expertise in composite materials.



Yifan Zhao (Senior Member, IEEE) was born in Zhejiang, China. He received the Ph.D. degree in automatic control and system engineering from the University of Sheffield, Sheffield, U.K., in 2007.

He is currently a Reader in Data Science with Cranfield University, Cranfield, U.K. His research interests include computer vision, signal processing, nondestructive testing, active thermography, and nonlinear system identification.



https://dspace.org/

Pattern recognition of barely visible impact damage in carbon composites using pulsed thermography

Zhou, Jia; Du, Weixiang; Yang, Lichao; Deng, Kailun; Addepalli, Sri ...

2021-12-13
IEEE
https://doi.org/10.1109/TII.2021.3134184
Zhou J, Du W, Yang L, et al., (2022) Pattern recognition of barely visible impact damage in carbon composites using pulsed thermography, IEEE Transactions on Industrial Informatics, Volume 18, Number 10, October 2022, pp. 7252-7261

Downloaded from a DSpace repository. https://dspace.org/